

# Energy- & Symmetry-Resolved Entanglement Dynamics in Disordered Bose-Hubbard Chain

Jie Chen,<sup>1,\*</sup> Chun Chen,<sup>1,†</sup> and Xiaoqun Wang<sup>1,2,3,4,‡</sup>

<sup>1</sup>Key Laboratory of Artificial Structures and Quantum Control (Ministry of Education),  
School of Physics and Astronomy, Shenyang National Laboratory for Materials Science,  
Shanghai Jiao Tong University, Shanghai 200240, China

<sup>2</sup>School of Physics, Zhejiang University, Hangzhou 310058, Zhejiang, China

<sup>3</sup>Tsung-Dao Lee Institute, Shanghai Jiao Tong University, Shanghai 200240, China

<sup>4</sup>Collaborative Innovation Center of Advanced Microstructures, Nanjing University, Nanjing 210093, China

(Dated: September 6, 2023)

A great deal of many-body localization (MBL) has been learnt from the one-dimensional (1D) spin or fermion systems where the carriers are sort of scatter particles. By contrast, the situation when multiple interacting bosons are clustered in a random potential remains much unexplored, albeit highly demanded. By using the numerical quantum quench dynamics, we study the symmetry-resolved entanglement entropy in a disordered Bose-Hubbard (dBH) chain, concentrating on the two types of inhomogeneous initial states to target the lower- and the higher-energy section of its dynamical phase diagram. From time-evolving a line-shape initial product state, we discover a hidden order: the sudden formation of the entropy imbalance across the different symmetry sectors, resulting in an entanglement-channel wave (ECW). Intriguingly, ECW melts in the strong-disorder limit. We conjecture the melting of ECW and the freezing of CDW are duo traits inherent to the disorder-induced MBL. Relatedly, a channel-resolved reanalysis hints the previously observed double-log growth of the number entropy may not indicate the breakdown of MBL for scatter particles. Through further exploiting the dynamical consequences of loading bosons onto one site, a cluster localization unique to the BH-type models emerges at the weak disorders. Collectively, the unraveled entanglement structures and dynamics manifest the dBH model's richness from a jointly energy- and symmetry-resolved perspective.

**Introduction.**—MBL comprises a paradigm of nonergodic eigenstate matter beyond Anderson insulator [1–7]. The interplay between randomness and interaction renders it essential to attack this nonequilibrium problem right from the level of many-body wavefunctions. Since the early days, entanglement entropy and its quench dynamics have been widely deployed to probe the slow albeit unrestricted information propagation in MBL [8–10]. A recent advance akin to this reasoning is the imposition of the symmetry resolution. Particularly, the ensuing symmetry-resolved entanglement dynamics has recently been measured using <sup>87</sup>Rb atoms to witness the logarithmic signature of MBL in dBH chains [11].

Despite being the paradigmatic model for interacting bosons, in the context of MBL, the dBH chain is much less explored than its fermionic counterpart, the spinless  $t$ - $V$  model, or equivalently, the Heisenberg  $XXZ$  chain via the Jordan-Wigner transformation. To our knowledge, even for the existing literature, the dynamical phase diagram of the dBH model has seldom been worked out. To this end, the central objective of this Letter is to construct and elucidate the dynamical phase diagram for the dBH model (see Fig. 1). On the one hand, as the scatter bosons are the low-energy carriers, the lower-lying portion of Fig. 1 resembles the whole phase diagrams of the typical disordered spin or fermion chains [13]. On the other hand, the higher-energy portion of Fig. 1 is unique to the bosonic systems (bosons cluster). This binary aspect of the phase diagram, originating from the quantum statistics properties of the model, demands that the dBH chain must be studied in an energy-resolved manner.

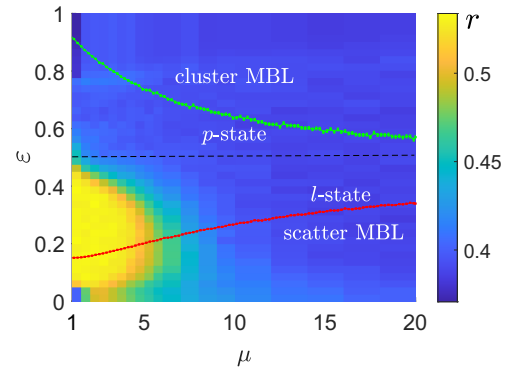


FIG. 1. Dynamical phase diagram of the periodic dBH model by contour plotting the averaged level-spacing ratio  $r$  [4, 12] of a chain with  $L = 12$ ,  $N = 6$ .  $\epsilon$  and  $\mu$  denote the eigenenergy density and the disorder strength. To minimize the interaction, the initial  $l$ -state consists of one (zero) boson on each site of the left (right) half-chain whose energy density is traced by the red line. To maximize the interaction, the initial  $p$ -state accommodates all bosons on the leftmost site, leaving the remainder unoccupied, whose energy density is delineated by the green line. Note that all bosons are released within the left half-chain, therefore the dominant tendencies of the particle flows in  $l$ - and  $p$ -states are unidirectional toward the right part.

We fuse together these two key ingredients, the symmetry resolution in the entanglement decomposition and the energy resolution in the initial-state preparation, as the correct method to scrutinize the quench dynamics for the important but understudied dBH model. Specifically,

a line-shape initial product state ( $l$ -state) is designed to access the lower-energy section of the phase diagram, where an ECW pops out in the coordinate plane of the symmetry index and time. Unlike the freezing of CDW, ECW symmetrizes in the strong-disorder limit. Although the fate of the disorder-induced MBL is still under intense debate [14, 15], the entropy symmetrization we propose relies on the symmetry and the strong disorders but not necessarily on the MBL phase itself, thus it could be more generic. Likewise, a point-shape initial product state ( $p$ -state) is devised to assess the higher-energy section of Fig. 1, where a cluster MBL is stabilized at the weak disorders, exhibiting the prolonged inhomogeneities in both particle and entropy distributions. As the mechanism underpinning the cluster MBL need not be the same as that for the MBL in spin or fermion systems, the challenges and critiques from the ongoing debate might not be immediately pertinent to the case at hand, thus leaving the door potentially open toward MBL in boson systems.

**Model & symmetry.**—The dBH chain is describable by the standard Hamiltonian,

$$H_{\text{dBH}} = -J \sum_i (a_i^\dagger a_{i+1} + \text{H.c.}) + \sum_i \frac{U}{2} n_i (n_i - 1) + \sum_i \mu_i n_i,$$

where  $a_i^\dagger$  ( $a_i$ ) is the boson creation (annihilation) operator at site  $i$ ,  $n_i = a_i^\dagger a_i$  ( $N = \sum_i n_i$ ) counts the local (total) boson occupation number,  $U$  parametrizes the on-site Hubbard interaction, and  $\mu_i \in [-\mu, \mu]$  is a diagonal random potential drawn from the box distribution. Crucially,  $[N, H_{\text{dBH}}] = 0$ , so the number-conserved dBH model respects the  $U(1)$  symmetry. In this work, all relevant quantities are averages over at least  $10^3$  random samples, solved by exact diagonalization [16] or Krylov-iterative method [17]. We set  $J = 1$  as the energy unit and fix  $U = 3J$ ,  $N = \frac{L}{2}$  in the succeeding numeric calculations.

Denote the total conserved operator as  $Q = Q_L + Q_R$  which is separable into two parts  $L$  and  $R$ , then for an eigenstate  $|\psi\rangle$  of  $Q$ , the reduced density matrix of  $L$ ,  $\rho_L = \text{Tr}_R(|\psi\rangle\langle\psi|)$ , commutes with  $Q_L$ , implying  $\rho_L = \bigoplus_n \rho_{L,n}$  where  $\rho_{L,n}$  the assembly of the blocks possessing the same eigenvalue  $n$  of  $Q_L$ . Because  $\sum_n \text{Tr}_{L,n} \rho_{L,n} = 1$ , for  $|\psi\rangle$ ,  $p_n = \text{Tr}_{L,n} \rho_{L,n}$  represents the probability of yielding eigenvalue  $n$  in the projective measurement of  $Q_L$ . Within that subspace, the normalized reduced density matrix assumes  $\tilde{\rho}_{L,n} = p_n^{-1} \rho_{L,n}$ . Consequently, the entanglement entropy of  $L$  decomposes into  $S_{\text{vN},L} = -\sum_n p_n \log_2 p_n + \sum_n p_n S_{\text{vN},L}^n$ , where  $S_{\text{vN},L}^n = -\text{Tr}_{L,n} \tilde{\rho}_{L,n} \log_2 \tilde{\rho}_{L,n}$  becomes the symmetry-resolved entanglement entropy for  $L$  accommodating  $n$  bosons.

Most previous works focus on the so-called number and configuration entropies,  $S_N = -\sum_n p_n \log_2 p_n$ ,  $S_C = \sum_n p_n S_{\text{vN},L}^n$ , which quantify the total entropies from the charge fluctuations across different sectors and the configurational superpositions within each sector weighted by probability [11, 18–25]. The drawback of using  $S_N$

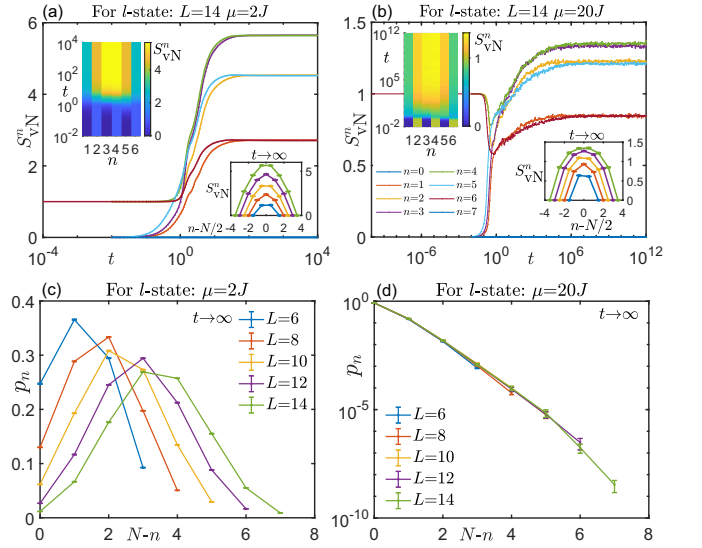


FIG. 2. Time evolution of the half-chain entanglement entropy from the initial  $l$ -state resolved into each symmetry channel labeled by the number index  $n$ . A periodic chain of length  $L$  and filling  $N = \frac{L}{2}$  is used. The top and bottom rows target  $S_{\text{vN},L}^n(t)$  and the scaling of  $p_{n,\infty}$  with  $L$ , while the left and right columns address the weak and strong disorders. Upper insets of (a),(b) illustrate the contour plots of  $S_{\text{vN},L}^n(t)$  in the  $(n,t)$  plane where the ECW and its melting are demonstrated. Lower insets of (a),(b) present the scaling of the saturation values of  $S_{\text{vN},L}^n$  at the infinite time (the  $n = 0, \frac{L}{2}$  components vanish identically). For illustration, error bars are preserved in the saturation results but omitted otherwise in the time evolutions.

and  $S_C$  is that they are not independent. Instead, we inspect the parsing of  $S_{\text{vN},L}$  into the set  $\{n, p_n, S_{\text{vN},L}^n\}$  where  $p_n$  is the absolute weight and  $S_{\text{vN},L}^n$  is determined by the relative weight. In terms of  $n$ , one can dynamically contrast  $S_{\text{vN},L}^{n'}$  where  $p_{n'}$  a maximum with  $S_{\text{vN},L}^{N-n'}$  where  $p_{N-n'}$  a minimum to uncover the pure entanglement structures beyond the usual scheme of space and time.

Experimentally, time evolutions for both  $p_n$  itself and a correlator  $C_n := \sum_{\{L_n\}} \sum_{\{R_{N-n}\}} |p(L_n \otimes R_{N-n}) - p(L_n)p(R_{N-n})|$  complementary to  $S_{\text{vN},L}^n$  were measured in [11]. Here,  $\{L_n\}$  ( $\{R_{N-n}\}$ ) denotes all possible configurations with  $n$  ( $N-n$ ) particles in the left (right) half-chain.  $C_n$  is not exactly  $S_{\text{vN},L}^n$ , but [11] suggests it might capture the qualitative characteristics of  $S_{\text{vN},L}^n$  through the quantification of the separability between  $L$  and  $R$ . In this regard, our predictions below may largely be observable.

**Create entanglement pattern in lower-energy section.**—Most quench studies of MBL start from nonentangled product states with predesigned local density imbalance imprinted [9, 26, 27]. As entanglement is absent from the start and usually builds up transiently in a continuous fashion, this construction appears structureless in the initial preparation of entanglement.

Curiously, can structural features of entanglement

evolve discontinuously from the product state at an infinitesimal lapse of time? Intriguingly, the symmetry-resolved entanglement entropy constitutes an ideal apparatus to address this question. Figures 2 and 3 show the entanglement growth resolved into each number sector in the numerical quantum quench experiment. Depending on how bosons are initially populated, two distinct dynamical patterns are observed.

Start from the  $l$ -state where the scatter bosons are the leading mobile identity, one novelty of the quench dynamics of entanglement is the discontinuous jump of  $S_{\text{VN},L}^n$  from 0 to 1 at  $t = 0^+$  (see [28] for a derivation). As demonstrated by Figs. 2(a),(b), for half-filled even chain with odd number of bosons and PBCs, all nontrivial  $S_{\text{VN},L}^n$  jump to 1 if  $n$  is even; for those odd  $n$ ,  $S_{\text{VN},L}^n$  instead develop smoothly from 0 up to the saturation. In analog to the CDW with local particle imbalance among even/odd lattice sites, based on the product line state, there arises a nonlocal entanglement imbalance among the symmetry channels  $n$  of the opposite parities.

**Entropy symmetrization in lower-energy section.**—One significance of the above finding pertains to scrutinize the influence of disorders. Will this ECW freeze in the localized phases? To set the stage, we first examine the thermal phases. As exemplified by Figs. 2(a),(c), it proves that in the weak-disorder regime for the initial  $l$ -state, both ECW and CDW melt to conform with ETH [29–32]. This is because under weak disorders, the reflection symmetry of the clean BH model is broken through a smooth manner, then for each eigenstate within the thermalization energy window, it follows  $S_{\text{VN},L}^{N-n} \approx S_{\text{VN},R}^{N-n}$ . Next, by virtue of  $S_{\text{VN},R}^{N-n} = S_{\text{VN},L}^n$ , valid for arbitrary pure states, one derives  $S_{\text{VN},L}^{N-n} \approx S_{\text{VN},L}^n$ , indicating the early-time even/odd- $n$  entanglement imbalance disappears at the long-time limit. Parallel rationale carries over to the infinite-time profile of  $p_n$  (denoted as  $p_{n,\infty}$ ): thermalization dictates the initially inhomogeneous boson population melts into the final uniform density landscape captured by a Gaussian.

Interestingly, we find for the initial  $l$ -state, this ECW symmetrizes with respect to channels  $n$  versus  $N - n$  even when subject to strong disorders [Fig. 2(b)], suggesting in scatter MBL, nonlocal ECW melts. Concurrently, the companion local boson occupations  $p_{n,\infty}$  remain frozen onto the initially asymmetric form [Fig. 2(d)], in accord with the localization phenomenon.

Assume the LIOM phenomenology for MBL [33–35], then the system's eigenstates at large  $\mu$  might be prescribable by filling the localized bits (l-bits). The diagonal approximation from taking the infinite-time limit then informs that the quasi-exponential decay of  $p_{n,\infty}$  as a function of  $n$  in Fig. 2(d) is determined by the projection coefficients of the initial  $l$ -state into these l-bit eigenstates. Via interpreting these expansion coefficients as the tunneling amplitudes, it is comprehensible that

the probability of the corresponding multi-boson tunneling processes is exponentially suppressed in the localized regime as per a measure set by the localization length.

One salient feature of Fig. 2 is the coexistence of the resemblance of  $\{S_{\text{VN},L}^n\}$  between (a),(b) with the contrast of  $\{p_{n,\infty}\}$  between (c),(d). A phenomenological argument for this disparate trend might run as follows. Take channels  $n = 1, 6$  in an  $L = 14$ ,  $N = 7$  chain as an example, then for a single sample, the use of the normalized  $\tilde{\rho}_{L,n}$  makes it possible to examine the relative arrangements of the component states within and between each individual channel of the pair. The overall discrepancy in the prefactors between the two is hidden. As (d) suggests the system is localized at  $\mu = 20$ , the dimensions of the pertinent nonzero blocks in  $\tilde{\rho}_{L,n=1,6}$  are controlled by the localization length. This constraint on the multi-boson configurations in each channel, combined with the minimization of the resultant energy mismatch, implies that these dominant density-matrix blocks might largely be diagonal. However, in view of the fact that (i) the  $n = 1$  channel is dominated by configurations with 3 bosons concentrated near the right and another 3 near the left entanglement cut and the remaining 1 localized at the middle of the left half-chain; (ii) the  $n = 6$  channel is dominated by configurations with 6 bosons evenly distributed along the left half-chain and 1 boson localized at either the left or the right cut; (iii) the onsite potentials  $\mu_i$  now represent large and uncorrelated random numbers, it is not guaranteed that within a single sample, the equality of the saturation values between  $S_{\text{VN},L}^{n=1,6}$  ensues. The observed entropy symmetrization in (b) thus hints that only after averaging over a sufficient amount

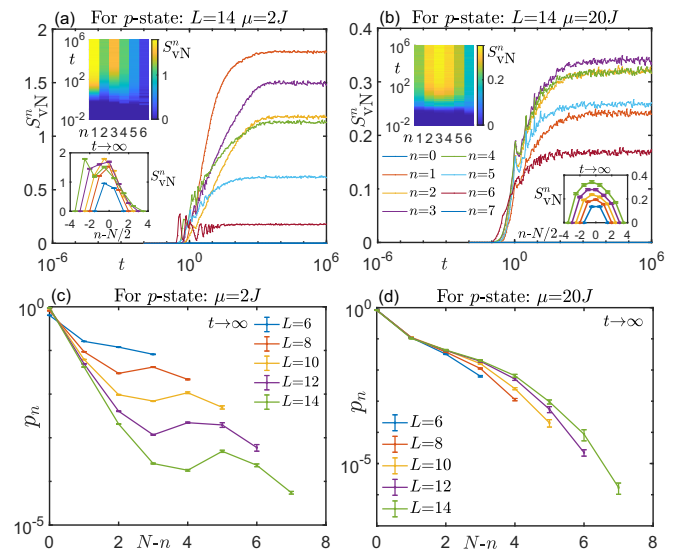


FIG. 3. Time evolution of the half-chain entanglement entropy from the initial  $p$ -state resolved into each symmetry channel labeled by  $n$ . Other arrangements are parallel to that of Fig. 2.

of random realizations, the statistical distributions of the eigenspectra of  $\tilde{\rho}_{L,n=1,6}$  tend to share some notable similarities. Analogous reasonings apply to other pairs of channels. Because the effective dimension of the leading nontrivial block in  $\tilde{\rho}_{L,n}$  increases as  $n$  approaches  $\frac{N}{2}$ , the saturation values of  $S_{\text{VN},L}^{n,N-n}$  get raised in a successive way. This is consistent with the overall tendency seen in (b).

**Entropy inhomogeneity in higher-energy section.**—Now we switch to the opposite extreme, the initial  $p$ -state, which maximizes the interaction. As displayed by Figs. 3(a),(c), in this case both the  $\{S_{\text{VN},L}^n\}$  evolution and the  $\{p_{n,\infty}\}$  distribution alter drastically at small  $\mu$ .

First, once all bosons are loaded onto a site, the Hubbard term dominates the Hamiltonian, which renders single-boson tunnelings quenched as perturbations. To reduce the energy mismatch, the time evolution of the  $p$ -state tends to preserve its cluster structure. Further, the neighboring eigenstates available to the  $p$ -state also share similar cluster features to sustain their comparable energy densities [28]. Consequently, within this high-energy window, the translation and reflection symmetries of the model are bound to be broken in an abrupt way by the small  $\mu$ . Numerically, Fig. 3(c) confirms the scaling trend of  $p_{n,\infty}$  toward this interaction-facilitated cluster localization at weak disorders upon increasing  $L$ .

Second, unlike the ECW formation in Figs. 2(a),(b), starting from the  $p$ -state,  $S_{\text{VN},L}^n$  grows continuously from zero and no ECW arises. Differing also from the long-time entropy symmetrizations in Figs. 2(a),(b), a strong entropy inhomogeneity develops in the cluster MBL region [Fig. 3(a)]. A qualitative justification for this may run as follows. Take channels  $n = 1, 6$  in an  $L = 14$ ,  $N = 7$  chain with small  $\mu$  as an example. According to Fig. 3(c), the  $n = 1$  channel is dominated by configurations with 6 bosons moved to near the left entanglement cut and 1 boson left within the left half-chain. While the  $n = 6$  channel is dominated by configurations with 6 bosons localized around the original site and 1 boson hopping across the left cut into the right half-chain. Because the leading energy mismatch between the initial  $p$ -state and the  $n = 6$  channel is small, any additional fluctuations induced by hoppings of single boson within the right half-chain are relatively important, thus these processes are restricted and the corresponding  $S_{\text{VN},L}^{n=6}$  gets suppressed. In comparison, the leading energy mismatch between the initial  $p$ -state and the  $n = 1$  channel is large, so comparatively, the fluctuations within the  $n = 1$  channel owing to the single-boson tunnelings along the left half-chain are less influential, suggesting the corresponding hopping processes are more extended, i.e., the size of the pertinent block in  $\tilde{\rho}_{L,n=1}$  increases. Accordingly, after normalization,  $S_{\text{VN},L}^{n=1}$  becomes enhanced. In this sense, it is the significant energy gap between channels  $n = 1, 6$ , together with its interplay with the weak disorders, that underpins the dynamics of cluster MBL [Figs. 3(a),(c)]. Other pairs

of channels can be addressed in a similar way. Through manipulating the initial  $p$ -state, we therefore find the equilibrated coexistence of the particle and entropy inhomogeneities in one unified dynamical setting.

Finally, the above picture carries over to the strongly-disordered circumstance with the addition that now each boson is localized by disorder as evident from Fig. 3(d), thus being confined to regions set by localization length. This explains why the entropy inhomogeneity is reduced at  $\mu = 20$  [Fig. 3(b)], in consistency with the entropy-symmetrization hypothesis for the disorder-driven MBL.

**Dynamic distinctions from  $S_N$  &  $S_C$ .**—For completeness, Fig. 4 summarizes the characteristics of the four types of quench dynamics thus far using the complementary evolutions of the number and configuration entropies [28].

Figures 4(a),(b) target the regime of small  $\mu$ . For the thermalization dome accessible via the  $l$ -state, besides reproducing the linear- $t$  and linear- $L$  scalings for the growth and saturation of  $S_C$  [inset of Fig. 4(b)], we find the temporal build-up of  $S_N$  obeys a log func-

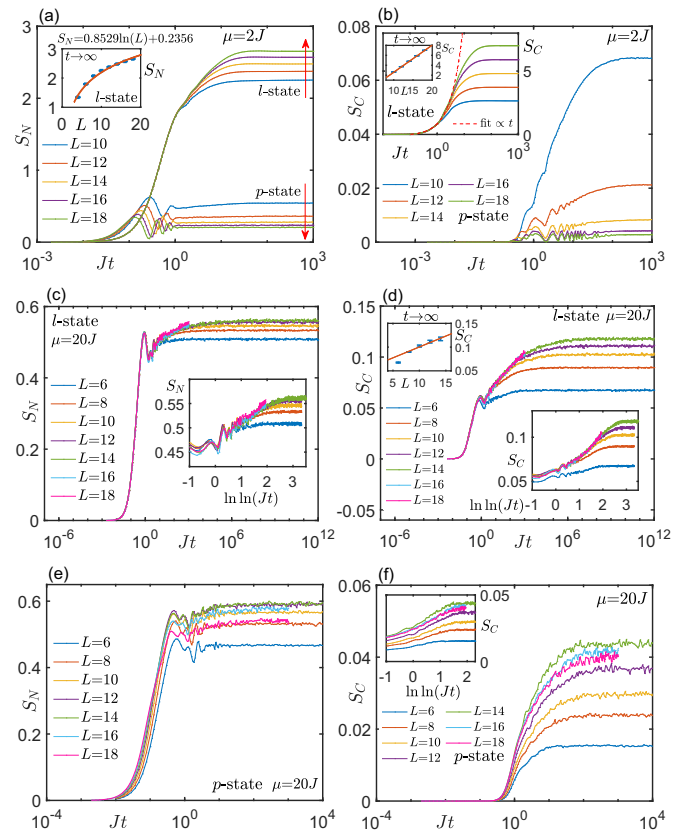


FIG. 4. Quench dynamics of the half-chain  $S_N$ ,  $S_C$ . The first row focuses on the weak-disorder regime where the scatter ETH and the cluster MBL are realizable by commencing from the  $l$ - and  $p$ -state. The second (third) row is devoted to the scatter (cluster) MBL at large  $\mu$ . To evolve the longer chains ( $L = 16, 18$ ), the Krylov-iterative method [17] is employed.



TABLE I. Dynamic  $S_N$ ,  $S_C$  characteristics for the dBH model.

phase		ETH	MBL			
			scatter	cluster		soft
				hard	area	
$S_N$	growth	$\ln t$	$\ln \ln t$	no	no	
	scaling	$\ln L$	area	area	area	
$S_C$	growth	$t$	$\ln t$	no	$\ln \ln t$	
	scaling	volume	volume	area	area	

tion of  $t$  and its saturation scales as a log function of  $L$  [Fig. 4(a)]. By contrast, once switch to the  $p$ -state, both the  $S_N$ ,  $S_C$  evolutions become halted and the scalings of their saturations fulfill the area law. The cluster MBL at small  $\mu$  hence features a bounded  $S_N$  growth and an interaction-stabilized entropy inhomogeneity. The latter never occurs in Anderson insulator. Figures 4(c)-(f) present the  $S_N$ ,  $S_C$  results for the strong-disorder regime. (c) shows that the  $S_N$  growth in scatter MBL follows a double-log function of  $t$ . Via a channel-resolved reanalysis, we show in [28] that the perceived particle-number fluctuations occur mainly as the reorganizations within the initial number channels where the particles are released rather than the substantial particle transports involving all available channels, in particular, those remote ones. In other words, the scaling of the  $S_N$  saturation is obedient to the area law. This is in accord with Fig. 2(d) but differs from the claim in [22, 24]. The companion  $\ln t$  rise of  $S_C$  in scatter MBL, along with its volume-law scaling, is revealed by (d). Interestingly, the cluster MBL at large  $\mu$  exhibits no appreciable temporal growth in  $S_N$ , which thereby obeys an area scaling law as evidenced by Fig. 4(e). The accompanying  $S_C$ , however, grows as a tentatively double-log function of  $t$ , but likely saturates to the area law as well at the long-time limit [Fig. 4(f)]. Table I recaps the features of  $S_N$ ,  $S_C$  to help differentiate between the four dynamical regions in the dBH chain.

**Summary & outlook.**—We numerically explore the energy-resolved dynamical phase diagram of the 1D dBH model using the quench evolutions of the symmetry-resolved entanglement entropies. By inspection on an ECW generated from an initial product state, we hypothesize an entropy symmetrization process for the strongly-disordered phases. One peculiarity of the dBH-type models revealed by the present work is the appearance of an MBL region formed by the clustered bosons.

In spite of the progress so far, several questions remain open regarding the analytic understanding on the mechanism of the ECW, its melting, and the description framework for the cluster MBL. Protocols on how to experimentally measure the symmetry-resolved entanglement entropies comprise another promising direction for the future study. These continued efforts will reveal more surprises founded upon the interplay among statistics, symmetry, entanglement, randomness, and interaction.

We thank Z. Cai for the insightful discussions. J.C. and X.W. were supported by MOST2022YFA1402701 and the NSFC Grant No. 11974244. C.C. was supported by a start-up fund from SJTU.

\* Corresponding author.  
chenjie666@sjtu.edu.cn

† Corresponding author.  
chunchen@sjtu.edu.cn

‡ Corresponding author.  
xiaoqunwang@zju.edu.cn

- [1] P. W. Anderson, Absence of Diffusion in Certain Random Lattices, *Phys. Rev.* **109**, 1492 (1958).
- [2] D. Basko, I. Aleiner, and B. Altshuler, Metal-insulator transition in a weakly interacting many-electron system with localized single-particle states, *Ann. Phys. (Amsterdam)* **321**, 1126 (2006).
- [3] I. V. Gornyi, A. D. Mirlin, and D. G. Polyakov, Interacting Electrons in Disordered Wires: Anderson Localization and Low- $T$  Transport, *Phys. Rev. Lett.* **95**, 206603 (2005).
- [4] V. Oganesyan and D. A. Huse, Localization of interacting fermions at high temperature, *Phys. Rev. B* **75**, 155111 (2007).
- [5] A. Pal and D. A. Huse, Many-body localization phase transition, *Phys. Rev. B* **82**, 174411 (2010).
- [6] R. Nandkishore and D. A. Huse, Many-Body Localization and Thermalization in Quantum Statistical Mechanics, *Annu. Rev. Condens. Matter Phys.* **6**, 15 (2015).
- [7] D. A. Abanin, E. Altman, I. Bloch, and M. Serbyn, Colloquium: Many-body localization, thermalization, and entanglement, *Rev. Mod. Phys.* **91**, 021001 (2019).
- [8] M. Žnidarič, T. Prosen, and P. Prelovšek, Many-body localization in the Heisenberg XXZ magnet in a random field, *Phys. Rev. B* **77**, 064426 (2008).
- [9] J. H. Bardarson, F. Pollmann, and J. E. Moore, Unbounded Growth of Entanglement in Models of Many-Body Localization, *Phys. Rev. Lett.* **109**, 017202 (2012).
- [10] M. Serbyn, Z. Papić, and D. A. Abanin, Universal Slow Growth of Entanglement in Interacting Strongly Disordered Systems, *Phys. Rev. Lett.* **110**, 260601 (2013).
- [11] A. Lukin, M. Rispoli, R. Schittko, M. E. Tai, A. M. Kaufman, S. Choi, V. Khemani, J. Léonard, and M. Greiner, Probing entanglement in a many-body-localized system, *Science* **364**, 256 (2019).
- [12] Y. Y. Atas, E. Bogomolny, O. Giraud, and G. Roux, Distribution of the Ratio of Consecutive Level Spacings in Random Matrix Ensembles, *Phys. Rev. Lett.* **110**, 084101 (2013).
- [13] D. J. Luitz, N. Laflorencie, and F. Alet, Many-body localization edge in the random-field Heisenberg chain, *Phys. Rev. B* **91**, 081103 (2015).
- [14] J. Šuntajs, J. Bonča, T. Prosen, and L. Vidmar, Quantum chaos challenges many-body localization, *Phys. Rev. E* **102**, 062144 (2020).
- [15] D. Abanin, J. Bardarson, G. De Tomasi, S. Gopalakrishnan, V. Khemani, S. Parameswaran, F. Pollmann, A. Potter, M. Serbyn, and R. Vasseur, Distinguishing localization from chaos: Challenges in finite-size systems, *Ann. Phys.* **427**, 168415 (2021).
- [16] J. M. Zhang and R. X. Dong, Exact diagonalization: the

- Bose–Hubbard model as an example, *European Journal of Physics* **31**, 591 (2010).
- [17] S. Paeckel, T. Köhler, A. Swoboda, S. R. Manmana, U. Schollwöck, and C. Hubig, Time-evolution methods for matrix-product states, *Annals of Physics* **411**, 167998 (2019).
- [18] M. Goldstein and E. Sela, Symmetry-Resolved Entanglement in Many-Body Systems, *Phys. Rev. Lett.* **120**, 200602 (2018).
- [19] J. C. Xavier, F. C. Alcaraz, and G. Sierra, Equipartition of the entanglement entropy, *Phys. Rev. B* **98**, 041106 (2018).
- [20] R. Bonsignori, P. Ruggiero, and P. Calabrese, Symmetry resolved entanglement in free fermionic systems, *J. Phys. A: Math. Theor.* **52**, 475302 (2019).
- [21] G. Perez, R. Bonsignori, and P. Calabrese, Quasiparticle dynamics of symmetry-resolved entanglement after a quench: Examples of conformal field theories and free fermions, *Phys. Rev. B* **103**, L041104 (2021).
- [22] M. Kiefer-Emmanouilidis, R. Unanyan, M. Fleischhauer, and J. Sirker, Evidence for Unbounded Growth of the Number Entropy in Many-Body Localized Phases, *Phys. Rev. Lett.* **124**, 243601 (2020).
- [23] D. J. Luitz and Y. B. Lev, Absence of slow particle transport in the many-body localized phase, *Phys. Rev. B* **102**, 100202 (2020).
- [24] M. Kiefer-Emmanouilidis, R. Unanyan, M. Fleischhauer, and J. Sirker, Slow delocalization of particles in many-body localized phases, *Phys. Rev. B* **103**, 024203 (2021).
- [25] N. Feldman and M. Goldstein, Dynamics of charge-resolved entanglement after a local quench, *Phys. Rev. B* **100**, 235146 (2019).
- [26] M. Schreiber, S. S. Hodgman, P. Bordia, H. P. Lüschen, M. H. Fischer, R. Vosk, E. Altman, U. Schneider, and I. Bloch, Observation of many-body localization of interacting fermions in a quasirandom optical lattice, *Science* **349**, 842 (2015).
- [27] D. J. Luitz, N. Laflorencie, and F. Alet, Extended slow dynamical regime close to the many-body localization transition, *Phys. Rev. B* **93**, 060201 (2016).
- [28] See the Supplemental Material for additional information.
- [29] J. M. Deutsch, Quantum statistical mechanics in a closed system, *Phys. Rev. A* **43**, 2046 (1991).
- [30] M. Srednicki, Chaos and quantum thermalization, *Phys. Rev. E* **50**, 888 (1994).
- [31] L. D’Alessio, Y. Kafri, A. Polkovnikov, and M. Rigol, From quantum chaos and eigenstate thermalization to statistical mechanics and thermodynamics, *Adv. Phys.* **65**, 239 (2016).
- [32] H. Kim, T. N. Ikeda, and D. A. Huse, Testing whether all eigenstates obey the eigenstate thermalization hypothesis, *Phys. Rev. E* **90**, 052105 (2014).
- [33] M. Serbyn, Z. Papić, and D. A. Abanin, Local Conservation Laws and the Structure of the Many-Body Localized States, *Phys. Rev. Lett.* **111**, 127201 (2013).
- [34] D. A. Huse, R. Nandkishore, and V. Oganesyan, Phenomenology of fully many-body-localized systems, *Phys. Rev. B* **90**, 174202 (2014).
- [35] V. Ros, M. Müller, and A. Scardicchio, Integrals of motion in the many-body localized phase, *Nucl. Phys. B* **891**, 420 (2015).

# Supplemental Material for “Energy- and Symmetry-Resolved Entanglement Dynamics in Disordered Bose-Hubbard Chain”

Jie Chen,<sup>1,\*</sup> Chun Chen,<sup>1,†</sup> and Xiaoqun Wang<sup>1,2,3,4,‡</sup>

<sup>1</sup>Key Laboratory of Artificial Structures and Quantum Control (Ministry of Education),  
School of Physics and Astronomy, Shenyang National Laboratory for Materials Science,  
Shanghai Jiao Tong University, Shanghai 200240, China

<sup>2</sup>School of Physics, Zhejiang University, Hangzhou 310058, Zhejiang, China

<sup>3</sup>Tsung-Dao Lee Institute, Shanghai Jiao Tong University, Shanghai 200240, China

<sup>4</sup>Collaborative Innovation Center of Advanced Microstructures, Nanjing University, Nanjing 210093, China

(Dated: September 6, 2023)

## CONTENTS

Supplemental Note 1. Time evolution of the channel-resolved number entropy	2
Supplemental Note 2. Dynamical generation of ECW in a $L = 4$ , $N = 2$ free-boson chain	3
Supplemental Note 3. Two types of melting processes of ECWs in the ETH phase	6
Supplemental Note 4. Comparison to the cut-varying entanglement patterns	7
Supplemental Note 5. Individual eigenstate properties at low and high eigenenergy densities under weak disorders	8
Supplemental Note 6. Analysis of the scaling behavior of $S_N$ initialized from the $l$ -state	9
Supplemental Note 7. Miscellaneous others	10

---

\* Corresponding author.  
[chenjie666@sjtu.edu.cn](mailto:chenjie666@sjtu.edu.cn)

† Corresponding author.  
[chunchen@sjtu.edu.cn](mailto:chunchen@sjtu.edu.cn)

‡ Corresponding author.  
[xiaoqunwang@zju.edu.cn](mailto:xiaoqunwang@zju.edu.cn)

### Supplemental Note 1. Time evolution of the channel-resolved number entropy

The reference [M. Kiefer-Emmanouilidis *et al.*, *Phys. Rev. Lett.* **124**, 243601 (2020)] reported that the total number entropy seems to grow double logarithmically over time even deep inside the MBL phase, hinting that the full localization might be unstable in the thermodynamic limit due to the unceasing particle or energy transports.

In this section, we perform a channel-resolved analysis of the total number entropy  $S_N$  for the disordered Bose-Hubbard (dBH) chain to help clarify the possibility that the observed double-log growth of  $S_N$  might not necessarily indicate the breakdown of the full localization.

The total number entropy  $S_N$  is defined by  $S_N(t) := -\sum_n p_n(t) \log_2 p_n(t)$ . This naturally suggests the channel-resolved number entropy  $S_N^n$  given by  $S_N^n(t) := -p_n(t) \log_2 p_n(t)$ .

Figure S1(b) shows the quantum quench evolutions of  $S_N^n(t)$  in a log-log format starting from the initial  $l$ -state for a strongly disordered ( $\mu = 20J$ ), periodic BH chain of length  $L = 18$ . There are two salient features from Fig. S1(b).

- First, the temporal  $S_N^n$  growth in those small  $n < 5$  channels fulfils a power law, which is much faster than  $\log \log(t)$ . While, for those large  $n > 5$  channels, the corresponding  $S_N^n$  growth does however become noticeably slower.
- Second, the absolute values of  $S_N^n$  in those small  $n < 5$  channels are negligibly smaller than the absolute values of  $S_N^n$  in those large  $n > 5$  channels. Particularly, it appears that the contributions from the channels  $n = 9, 8$  dominate the whole time evolution of the total  $S_N(t)$ .

From Fig. 4(c) in the main text, we have known that the total  $S_N$  in this quantum quench setup indeed grows double logarithmically over time. Therefore, combine the above-listed two points, we argue that the double-log growth of  $S_N$  should be predominantly controlled by the channels of large  $n = 9, 8$  and the participation of those small- $n$  channels might be negligible. In other words, in this quantum quench evolution, particles are well confined to the left half-chain; the perceived particle-number fluctuations occur mainly as reorganizations within the initial number channels where particles are first released rather than the substantial particle transports involving all available channels, in particular, those remote channels of small  $n$ .

As a comparison, Fig. S1(a) plots the channel-resolved buildup of  $S_N^n$  for the weak-disorder thermal regime, where we still begin with the initial  $l$ -state and now set  $\mu = 2J$ . The obtained results are consistent with the predictions of ETH, namely, each channel participates significantly and almost equally. As per Fig. 4(a) in the main text, the overall growth of the total  $S_N$  in this case follows a logarithmic function of time. This might be due to the fact that after the transient period, the paired two channels  $n'$  and  $N - n'$  could exhibit the opposite evolution tendencies before eventually converging to the same saturation value. Particularly, for those large- $n$  channels, the corresponding  $S_N^n$  experiences first an increase and then a decrease over time before reaching the saturation, which is unlike the monotonic increase of  $S_N^n$  occurring in those small- $n$  channels.

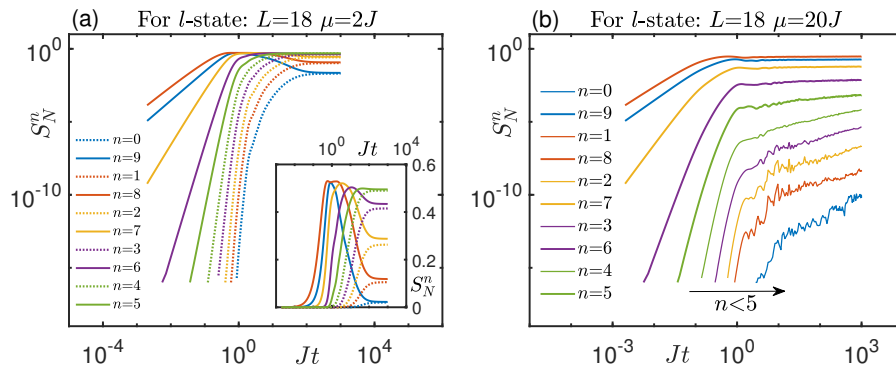


FIG. S1. Time evolution of the channel-resolved number entropy  $S_N^n$ . Here we start from the initial  $l$ -state in a disordered, periodic BH chain of length  $L = 18$ . (a) gives the results for the thermal phase realized at the weak-disorder regime of  $\mu = 2J$ . (b) corresponds to the regime deep inside the scatter MBL phase stabilized by  $\mu = 20J$ .



**Supplemental Note 2. Dynamical generation of ECW in a  $L = 4$ ,  $N = 2$  free-boson chain**

The formation of the entanglement channel wave (ECW) can be mathematically established on a finite free-boson chain. Here, for the purpose of illustration, it might be illuminating to work out some details for the simplest case where two bosons hop freely on a four-site periodic chain. The tight-binding model is described by the following Hamiltonian,

$$H_0 = -J \sum_{i=1}^L (a_i^\dagger a_{i+1} + \text{H.c.}) = -2J \sum_k \cos k a_k^\dagger a_k, \quad (\text{S1})$$

where the lattice constant is set to 1 and the Fourier transform reads  $a_i = L^{-\frac{1}{2}} \sum_k e^{ikR_i} a_k$ .

Starting from a normalized pure state  $|\psi\rangle = \sum_{a,b} \psi_{a,b} |a\rangle |b\rangle$  where  $\{|a\rangle\}, \{|b\rangle\}$  are orthonormal bases for the left and right half-chains, the reduced density matrix is simply given by

$$\rho_L = \text{Tr}_R (|\psi\rangle \langle \psi|) = \sum_{a,a'} \left[ \sum_{b'} \psi_{a,b'} \psi_{a',b'}^* \right] |a\rangle \langle a'|. \quad (\text{S2})$$

Under the unitary time evolution, it is easy to see that

$$\psi_{a,b} = \langle a, b | \psi \rangle \implies \psi_{a,b}(t) = \langle a, b | e^{-iH_0 t} | \psi \rangle. \quad (\text{S3})$$

Now the symmetry-resolved density matrix  $\rho_{L,n}$  can be constructed by specifying and going through all basis states  $|a, b\rangle$  within the number sectors  $n$  and  $N - n$ . For the case of  $L = 4$ ,  $N = 2$ , it is easy to see that  $n = 0, 1, 2$  and due to the observation that  $\rho_{L,n=0,2}$  are essentially one dimensional, the corresponding  $S_{vN,L}^{n=0,2} = 0$ . We thus only need to examine the nontrivial channel  $n = 1$ . The basis state can then be labelled by the site index where the single boson is located. Concretely,

$$(a, b) = (1, 3), (1, 4), (2, 3), (2, 4), \quad (\text{S4})$$

where for instance  $(a, b) = (1, 3)$  means that  $|a, b\rangle = a_1^\dagger a_3^\dagger |0\rangle$ .

The initial  $l$ -state can be written as follows,

$$|\psi\rangle = a_1^\dagger a_2^\dagger |0\rangle. \quad (\text{S5})$$

Upon Fourier transforms, one derives

$$e^{-iH_0 t} |\psi\rangle = L^{-2} \sum_{k,k'} \sum_{R_i, R_j} e^{-ikR_1} e^{-ik'R_2} e^{i(2J \cos k + 2J \cos k')t} e^{ikR_i} e^{ik'R_j} a_i^\dagger a_j^\dagger |0\rangle. \quad (\text{S6})$$

Throughout this note we always assume that  $t \geq 0$ . Inserting the component basis state from channel  $n = 1$ , Eq. (S3) then yields

$$(a, b) = (1, 3) \implies \psi_{1,3}(t) = L^{-2} \sum_{k,k'} \left( e^{-ik'(R_2 - R_3)} + e^{-ik(R_1 - R_3)} e^{-ik'(R_2 - R_1)} \right) \cdot e^{i(2J \cos k + 2J \cos k')t}, \quad (\text{S7})$$

$$(a, b) = (1, 4) \implies \psi_{1,4}(t) = L^{-2} \sum_{k,k'} \left( e^{-ik'(R_2 - R_4)} + e^{-ik(R_1 - R_4)} e^{-ik'(R_2 - R_1)} \right) \cdot e^{i(2J \cos k + 2J \cos k')t}, \quad (\text{S8})$$

$$(a, b) = (2, 3) \implies \psi_{2,3}(t) = L^{-2} \sum_{k,k'} \left( e^{-ik(R_1 - R_3)} + e^{-ik(R_1 - R_2)} e^{-ik'(R_2 - R_3)} \right) \cdot e^{i(2J \cos k + 2J \cos k')t}, \quad (\text{S9})$$

$$(a, b) = (2, 4) \implies \psi_{2,4}(t) = L^{-2} \sum_{k,k'} \left( e^{-ik(R_1 - R_4)} + e^{-ik(R_1 - R_2)} e^{-ik'(R_2 - R_4)} \right) \cdot e^{i(2J \cos k + 2J \cos k')t}. \quad (\text{S10})$$

Clearly, all the above four elements vanish identically at  $t = 0$ .

Taking advantage of the periodicity of momenta  $k, k'$ , it is ready to show that

$$\psi_{1,3}^*(t) = \left\{ L^{-2} \sum_{k,k'} \left[ e^{ik'} + e^{2ik} e^{-ik'} \right] \cdot e^{i(2J \cos k + 2J \cos k')t} \right\}^*$$

$$\begin{aligned}
&= L^{-2} \sum_{k,k'} \left[ e^{-ik'} + e^{-2ik} e^{ik'} \right] \cdot e^{-i(2J \cos k + 2J \cos k')t} \\
&= L^{-2} \sum_{k,k'} \left[ e^{-i(k'+\pi)} + e^{-2i(k+\pi)} e^{i(k'+\pi)} \right] \cdot e^{i(2J \cos k + 2J \cos k')t} \\
&= -L^{-2} \left\{ \sum_{k,k'} \left[ e^{-ik'} + e^{-2ik} e^{ik'} \right] \cdot e^{i(2J \cos k + 2J \cos k')t} \right\} \\
&= -L^{-2} \left\{ \sum_{k,k'} \left[ e^{ik'} + e^{2ik} e^{-ik'} \right] \cdot e^{i(2J \cos k + 2J \cos k')t} \right\} = -\psi_{1,3}(t). \tag{S11}
\end{aligned}$$

Therefore, after switching the signs of  $k, k'$ , it is shown that  $\psi_{1,3}(t)$  is purely imaginary, i.e.,  $\psi_{1,3}^*(t) = -\psi_{1,3}(t)$ . By contrast, one finds that  $\psi_{1,4}(t)$  is purely real,

$$\begin{aligned}
\psi_{1,4}^*(t) &= \left\{ L^{-2} \sum_{k,k'} \left[ e^{2ik'} + e^{3ik} e^{-ik'} \right] \cdot e^{i(2J \cos k + 2J \cos k')t} \right\}^* \\
&= L^{-2} \sum_{k,k'} \left[ e^{-2ik'} + e^{-3ik} e^{ik'} \right] \cdot e^{-i(2J \cos k + 2J \cos k')t} \\
&= L^{-2} \sum_{k,k'} \left[ e^{-2i(k'+\pi)} + e^{-3i(k+\pi)} e^{i(k'+\pi)} \right] \cdot e^{i(2J \cos k + 2J \cos k')t} \\
&= L^{-2} \sum_{k,k'} \left[ e^{-2ik'} + e^{-3ik} e^{ik'} \right] \cdot e^{i(2J \cos k + 2J \cos k')t} \\
&= L^{-2} \sum_{k,k'} \left[ e^{2ik'} + e^{3ik} e^{-ik'} \right] \cdot e^{i(2J \cos k + 2J \cos k')t} = \psi_{1,4}(t). \tag{S12}
\end{aligned}$$

Therefore,  $\psi_{1,4}^*(t) = \psi_{1,4}(t)$ . Furthermore, one can show that  $\psi_{1,3}(t) = \psi_{2,4}(t)$ ,

$$\begin{aligned}
\psi_{2,4}(t) &= L^{-2} \sum_{k,k'} \left[ e^{3ik} + e^{ik} e^{2ik'} \right] \cdot e^{i(2J \cos k + 2J \cos k')t} \\
&= L^{-2} \sum_{k',k} \left[ e^{3ik'} + e^{ik'} e^{2ik} \right] \cdot e^{i(2J \cos k' + 2J \cos k)t} \\
&= L^{-2} \sum_{k',k} \left[ e^{-3ik'} + e^{-ik'} e^{2ik} \right] \cdot e^{i(2J \cos k' + 2J \cos k)t} \\
&= L^{-2} \sum_{k',k} \left[ e^{4ik'} e^{-3ik'} + e^{-ik'} e^{2ik} \right] \cdot e^{i(2J \cos k' + 2J \cos k)t} = \psi_{1,3}(t), \tag{S13}
\end{aligned}$$

where in the second line we exchange  $k \rightleftharpoons k'$ , switch the sign of  $k'$  only in the third line, and finally use the identity that  $e^{ik'L} = e^{4ik'} = 1$ . Likewise, we can show that  $\psi_{1,4}(t) = \psi_{2,3}(t)$ ,

$$\begin{aligned}
\psi_{2,3}(t) &= L^{-2} \sum_{k,k'} \left[ e^{2ik} + e^{ik} e^{ik'} \right] \cdot e^{i(2J \cos k + 2J \cos k')t} \\
&= L^{-2} \sum_{k',k} \left[ e^{2ik'} + e^{ik'} e^{ik} \right] \cdot e^{i(2J \cos k' + 2J \cos k)t} \\
&= L^{-2} \sum_{k',k} \left[ e^{-2ik'} + e^{-ik'} e^{-ik} \right] \cdot e^{i(2J \cos k' + 2J \cos k)t} \\
&= L^{-2} \sum_{k',k} \left[ e^{-2ik'} e^{4ik'} + e^{-ik'} e^{-ik} e^{4ik} \right] \cdot e^{i(2J \cos k' + 2J \cos k)t} = \psi_{1,4}(t), \tag{S14}
\end{aligned}$$

where in the second line we exchange  $k \rightleftharpoons k'$ , switch both signs of  $k, k'$  in the third line, and finally use the identity that  $e^{ik'L} = e^{4ik'} = e^{ikL} = e^{4ik} = 1$ .

To summarize, by resorting to the system's translation and reflection symmetries, we find that

$$\psi_{1,3}^*(t) = -\psi_{1,3}(t), \tag{S15}$$

$$\psi_{1,4}^*(t) = \psi_{1,4}(t), \quad (\text{S16})$$

$$\psi_{1,3}(t) = \psi_{2,4}(t), \quad (\text{S17})$$

$$\psi_{1,4}(t) = \psi_{2,3}(t). \quad (\text{S18})$$

Armed with the above relations, the symmetry-resolved density matrix  $\rho_{L,n=1}(t)$  can be readily constructed as per Eq. (S2) as a two-by-two matrix,

$$\begin{aligned} \rho_{L,n=1}(t) &:= \begin{bmatrix} \rho_{1,1}(t) & \rho_{1,2}(t) \\ \rho_{2,1}(t) & \rho_{2,2}(t) \end{bmatrix} = \begin{bmatrix} \psi_{1,3}(t) & \psi_{1,4}(t) \\ \psi_{2,3}(t) & \psi_{2,4}(t) \end{bmatrix} \cdot \begin{bmatrix} \psi_{1,3}^*(t) & \psi_{2,3}^*(t) \\ \psi_{1,4}^*(t) & \psi_{2,4}^*(t) \end{bmatrix} \\ &= \begin{bmatrix} \psi_{1,3}(t)\psi_{1,3}^*(t) + \psi_{1,4}(t)\psi_{1,4}^*(t) & \psi_{1,3}(t)\psi_{2,3}^*(t) + \psi_{1,4}(t)\psi_{2,4}^*(t) \\ \psi_{2,3}(t)\psi_{1,3}^*(t) + \psi_{2,4}(t)\psi_{1,4}^*(t) & \psi_{2,3}(t)\psi_{2,3}^*(t) + \psi_{2,4}(t)\psi_{2,4}^*(t) \end{bmatrix} \\ &= [\psi_{1,3}(t)\psi_{1,3}^*(t) + \psi_{1,4}(t)\psi_{1,4}^*(t)] \cdot \begin{bmatrix} 1 & 0 \\ 0 & 1 \end{bmatrix}, \end{aligned} \quad (\text{S19})$$

where the following relations are employed,  $\psi_{1,3}(t)\psi_{2,3}^*(t) + \psi_{1,4}(t)\psi_{2,4}^*(t) = \psi_{1,3}(t)\psi_{1,4}^*(t) + \psi_{1,4}(t)\psi_{1,3}^*(t) = 0$  and  $\psi_{2,3}(t)\psi_{2,3}^*(t) + \psi_{2,4}(t)\psi_{2,4}^*(t) = \psi_{1,4}(t)\psi_{1,4}^*(t) + \psi_{1,3}(t)\psi_{1,3}^*(t)$ . Therefore, assume that  $|\psi_{1,3}|^2 + |\psi_{1,4}|^2 \neq 0$ , the normalized density matrix for the channel  $n = 1$  is simply

$$\tilde{\rho}_{L,n=1}(t > 0) = \begin{bmatrix} \frac{1}{2} & 0 \\ 0 & \frac{1}{2} \end{bmatrix} \implies S_{\text{vN},L}^{n=1}(t > 0) = -\frac{1}{2} \log_2 \left( \frac{1}{2} \right) - \frac{1}{2} \log_2 \left( \frac{1}{2} \right) = 1. \quad (\text{S20})$$

In other words, once  $t$  starts to deviate from 0,  $S_{\text{vN},L}^{n=1}(t)$  will suddenly jump to 1 and largely become a constant (up to abrupt drops at particular periodicities due to the vanishing of the diagonal element) in this simplest nontrivial setting.

One peculiarity associated to the dynamics of symmetry-resolved entanglement entropy as encoded in Eqs. (S19) and (S20) is that at any moment  $t$ , regardless how small the diagonal matrix element  $|\psi_{1,3}|^2 + |\psi_{1,4}|^2 \geq 0$  is, once it is nonzero, the equality of the dominant diagonal elements  $\rho_{1,1}$  and  $\rho_{2,2}$  guarantees that  $S_{\text{vN},L}^{n=1} = 1$ . Via this demonstration, the existence of ECW can thus be rigorously established.

It is easy to show that for the free-fermion hopping model, Eqs. (S15) to (S18) change to

$$\psi_{1,3}^*(t) = -\psi_{1,3}(t), \quad (\text{S21})$$

$$\psi_{1,4}^*(t) = \psi_{1,4}(t), \quad (\text{S22})$$

$$\psi_{1,3}(t) = -\psi_{2,4}(t), \quad (\text{S23})$$

$$\psi_{1,4}(t) = -\psi_{2,3}(t). \quad (\text{S24})$$

However, the following two key equalities still hold,  $\psi_{1,3}(t)\psi_{2,3}^*(t) + \psi_{1,4}(t)\psi_{2,4}^*(t) = -\psi_{1,3}(t)\psi_{1,4}^*(t) - \psi_{1,4}(t)\psi_{1,3}^*(t) = 0$  and  $\psi_{2,3}(t)\psi_{2,3}^*(t) + \psi_{2,4}(t)\psi_{2,4}^*(t) = \psi_{1,4}(t)\psi_{1,4}^*(t) + \psi_{1,3}(t)\psi_{1,3}^*(t)$ , therefore the same ECW appears in the fermion systems as well.

### Supplemental Note 3. Two types of melting processes of ECWs in the ETH phase

In this work, we exclusively focus on the even chains at half filling with periodic boundary conditions. Under these specifications, we find there exist two types of ECWs depending on the parity of the total number of bosons. As shown by Figs. S2(a),(b), when the total number of bosons is even, the discontinuous jumps of  $S_{vN,L}^n$  occurs only for those odd- $n$  channels. In comparison, as shown by Figs. S2(c),(d), when the total number of bosons is odd, the discontinuous jumps of  $S_{vN,L}^n$  occurs only for those even- $n$  channels. Here we always start from the  $l$ -state and choose the disorder strength  $\mu = 2J$  to be small.

To be pedantic, we should name the ECW in Figs. S2(a),(b) to be the reflection-symmetric ECW (with respect to the channel axis  $n$ ). While, the ECW in Figs. S2(c),(d) should be called the reflection-asymmetric ECW for the obvious geometric reasons.

Due to the weak breaking of the spatial reflection symmetry, we know these two types of ECWs will melt in the long-time limit. Figure S2 reveals that the melting processes for these two ECWs are different.

Concretely, from Figs. S2(a),(b), we observe that for the reflection-symmetric ECW, the  $\mathbb{Z}_2$  channel wave pattern disappears but the channel reflection symmetry of the ECW persists. By contrast, from Figs. S2(c),(d), we observe that for the reflection-asymmetric ECW, the disappearance of the  $\mathbb{Z}_2$  channel wave is accompanied by a symmetrization process with the emergence of the channel reflection symmetry. Note that this channel reflection symmetry does not exist in the initially reflection-asymmetric ECW. In this sense, the melting of the reflection-asymmetric ECW is more drastic than that of the reflection-symmetric ECW.

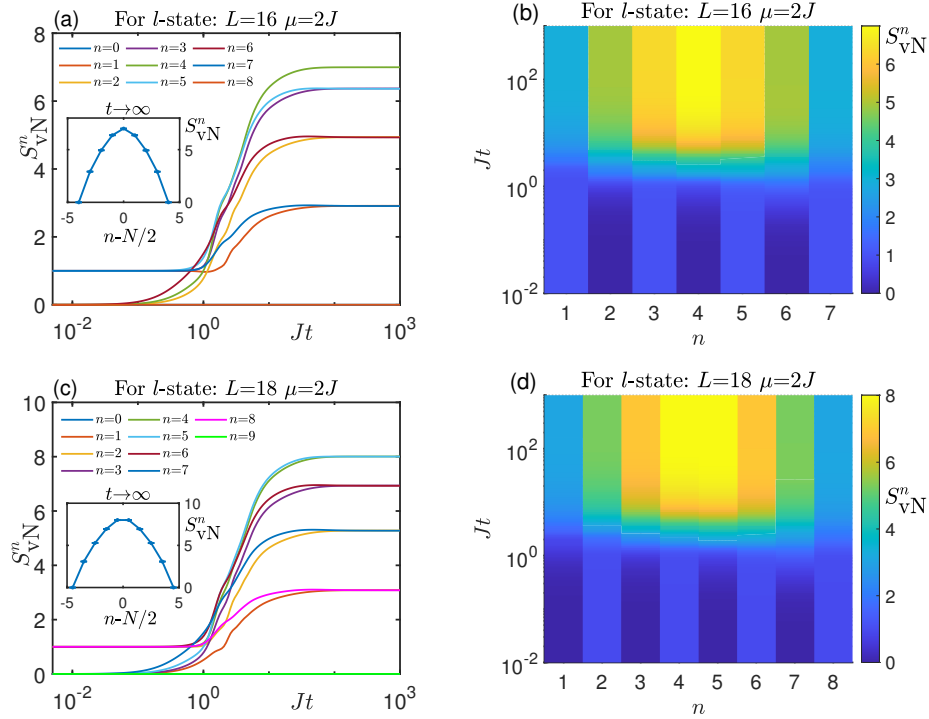


FIG. S2. Two types of ECWs and their different melting processes in the thermal regime. (a),(b) show the formation and the time evolution of the channel-reflection-symmetric ECW in a periodic even chain accommodating even number of total bosons. The melting of this first type of ECW removes the  $\mathbb{Z}_2$  channel wave pattern but preserves the channel reflection symmetry. (c),(d) show the formation and the time evolution of the channel-reflection-asymmetric ECW in a periodic even chain accommodating odd number of total bosons. The melting of this second type of ECW not only removes the  $\mathbb{Z}_2$  channel wave pattern but also allows for the emergence of the channel reflection symmetry.

#### Supplemental Note 4. Comparison to the cut-varying entanglement patterns

When devising the pattern of entanglement, one usually wants to maximize the inherent nonlocality structure as much as possible. By fixing one cut position at the middle of the chain and the other at the boundary, the ECW based on the half-chain von Neumann entanglement entropy maintains the maximal degree with regard to nonlocality.

Conceptually, the simplest entanglement pattern one may think of is by successively varying the cut position from the first bond at the boundary to the middle bond at the chain's centre. A representative for this type of real-space entanglement patterns is provided by the dimer product state of spin chains, i.e., two nearest spins are first entangled into a singlet and next this two-spin dimer forms the product state with other similar two-spin dimers. This dimer-like entanglement pattern resembles the CDW; one only needs to change the position variable from the site to the bond.

However, as compared to the ECW, the nonlocality property of such an initial-state arrangement is reduced in two aspects. First, for the ideal case of the dimer product state, one can easily understand that the nonlocality property is somehow minimized because the actual entanglement of the state only involves two nearest-neighboring sites. Second, the varying of the cut position necessarily creates some inhomogeneity of the entanglement pattern because the nonlocality feature and the corresponding entanglement entropy have to diminish monotonically when one of the cuts is moved away from the centre bond of the chain to its end bond.

In the main text, we stress that the normalization is not only a crucial conceptual step for the proper definition of the symmetry-resolved entanglement entropy, but it also comprises an indispensable technical procedure to hide the absolute smallness of the pertinent density-matrix elements [for example see Eqs. (S19) and (S20)] such that the ECW pattern determined from the relative weights within the number-symmetry block can surface. By contrast, this normalization procedure does not arise in the calculation of the cut-varying entanglement patterns such as the aforementioned dimer product state and the like. Therefore, in view of the exponential suppression of the particle transport under the strong disorders, we anticipate that the many-body dephasing would not be efficient enough to symmetrize the real-space cut-varying entanglement patterns.

Roughly speaking, the preservation of CDW in MBL is due to its finite overlaps with the local integrals of motion (l-bits) configurations. This physical reasoning works well to interpret the imbalanced distribution of  $p_{n,\infty}$ . However, the same rationale might not be directly applicable to account for the situation of ECW. This is partly owing to the intrinsic nonlocality of ECW. But, more importantly, unlike the significance of the absolute projection amplitudes onto these l-bit states for the persistence of the initial CDW or  $p_{n,\infty}$ , it is the relative weights among those nonlocal l-bit projections that control the evolution of ECW.

Likewise, the physical picture based on the Hilbert-space (de)localization may also be largely set by the absolute values of the prefactors associated to the generated component states under the unitary time evolution of the initial state. In this sense, the calculation of the accompanying IPR could be useful in understanding the  $p_{n,\infty}$  distribution. Nonetheless, it might not directly concern the symmetrization between  $S_{\text{vN},L}^{n,N-n}$ . Symmetry-resolved IPRs may be a useful alternative for this purpose.



### Supplemental Note 5. Individual eigenstate properties at low and high eigenenergy densities under weak disorders

The purpose of this section is to exhibit the observation that the eigenstates formed by scatter bosons could be drastically different from the eigenstates formed by cluster bosons. To this end, we concentrate on the region of weak disorder strength ( $\mu = 2J$ ), pick up an arbitrary random sample, and then perform an analysis upon the individual eigenstates in an energy-density resolved manner. As  $\mu$  is small, we do not expect any significant differences between different random-sample realizations.

Figure S3(a) displays the channel-resolved  $S_{\text{VN},L}^n$  as a function of the channel index  $n$  for the eleven eigenstates of the Hamiltonian  $H_{\text{dBH}}$  whose eigenenergies are the closest to that of the initial  $l$ -state  $|l\rangle$ , i.e., the eleven closest to  $\langle l|H_{\text{dBH}}|l\rangle \sim 0.25$ . Note that here we just pick up one arbitrary random-sample realization. Clearly, these eleven curves nicely overlap with each other, demonstrating the agreement with the eigenstate thermalization hypothesis (ETH), viz., the wavefunction properties in this low-energy window are chiefly controlled by the specified eigenenergy density. Therefore, in this ETH regime, any arbitrary eigenstate could be the representative to extract the relevant physical quantities about the system. It is worth emphasizing that these eleven low-energy eigenstates like the  $l$ -state are comprised mainly by scatter bosons.

However, once we switch to the regime of the high-energy  $p$ -state  $|p\rangle$ , Fig. S3(b) presents the corresponding expectation value of the local boson occupation number as a function of the site index  $i$ . Here, as is in panel (a), we pick up eleven eigenstates from an arbitrary random sample whose eigenenergies are the closest to that of the initial  $p$ -state, i.e., the eleven closest in energy to  $\langle p|H_{\text{dBH}}|p\rangle \sim 0.75$ . Strikingly, we find that within this high-energy window, each eigenstate exhibits distinguishable properties. First, almost all bosons in each eigenstates cluster round a particular single lattice site and second, for distinct eigenstates, the sites where the clustered bosons sit are also different. In other words, in this high-energy window, the ETH breaks down, in the sense that although two eigenstates are adjacent in eigenenergy, their physical properties could be dramatically distinct from each other. To some extent, Fig. S3(b) illustrates the Hilbert-space structure that allows for the formation of the cluster MBL in the presence of weak disorders.

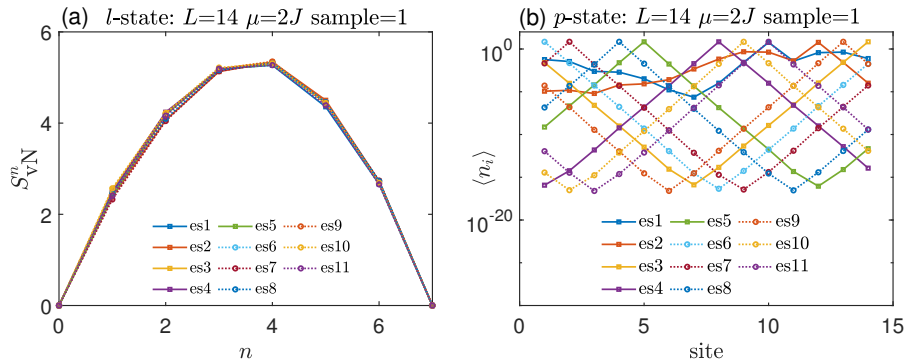


FIG. S3. Individual eigenstate properties at the low- and high-energy densities. (a) depicts the channel-resolved entropy  $S_{\text{VN},L}^n$  as a function of the channel index  $n$  for the eleven eigenstates which are the closest in energy to that of the initial  $l$ -state. As the  $l$ -state is formed by scatter bosons, (a) gives the results for the low-energy window, which is consistent with the predictions based on ETH. (b) depicts the local boson occupation number as a function of the lattice site for the eleven eigenstates which are the closest in energy to that of the initial  $p$ -state. As the  $p$ -state is formed by cluster bosons, (b) supplies the results from the high-energy window, which clearly violate the predictions based on ETH. Notice that here no disorder averages are needed, because only one arbitrary random-sample realization is used. The length of the periodic chain is 14, the total number of bosons is 7, and the disorder strength  $\mu = 2J$ .

**Supplemental Note 6. Analysis of the scaling behavior of  $S_N$  initialized from the  $l$ -state**

For the later convenience, let  $n_r = N - n$  denote the number of particles in the right half-chain,  $n$  denote the number of particles in the left half-chain, and  $N = L/2$  denote the total number of particles in the whole chain.

The  $l$ -state, whose energy density is in the ETH region, thermalizes at small disorder. As shown by Fig. S4(a), the corresponding long-time  $p_{n_r}$  does approximately satisfy the Gaussian distribution. One can thus assume that  $p_{n_r} = \alpha \cdot e^{-(n_r - N/2)^2/\beta^2}$ . Further, since  $p_{n_r}$  needs to be normalized, as compared to the normalized Gaussian distribution, it is derivable that  $\beta \sim N$  and  $\alpha \sim \frac{1}{N}$ . According to Fig. 2(c) in the main text, it is then reasonable to let  $\beta \approx cL$  and  $\alpha \approx d\frac{1}{L}$ , where  $c, d$  are two parameters. Therefore, the particle number entropy  $S_N$  can be calculated as follows,

$$\begin{aligned} S_N &= \sum_{n_r=0}^N -p_{n_r} \cdot \log(p_{n_r}) = -\log(\alpha) + \frac{\alpha}{\beta^2} 2 \sum_{n_r=0}^{N/2} \left[ n_r^2 e^{-n_r^2/\beta^2} \right] \\ &\approx -\log(\alpha) + \frac{\alpha}{\beta^2} 2 \int_0^{N/2} n_r^2 e^{-n_r^2/\beta^2} dn_r \\ &= \log(L) - \log(d) + \frac{1}{4}d \left[ 2c\sqrt{\pi} \text{Erf} \left( \frac{1}{4c} \right) - e^{-1/16c^2} \right]. \end{aligned} \quad (\text{S25})$$

We see that  $S_N \sim \ln(L)$ . This is also verified by the numerical results given in Fig. S4(c).

For a free bosonic system without interactions, an ideal case can be assumed where the various possible configurations are assumed to have the same probability in the thermalized state, which means that  $p_n$  is determined only by the Hilbert-space dimension of the chunk. The total Hilbert space of a bosonic system with chain length  $L$  and the number of particles  $N$  is  $D_N^L = \frac{(L+N-1)!}{N!(L-1)!}$ , the dimension of the Hilbert subspace with particle number  $n$  on the left half-chain is  $D_n = D_n^{L/2} D_{N-n}^{L/2}$ , so  $p_n = D_n/D_N^L$ . For the current half-filling system  $N = L/2$ , the result of the numerical calculation is shown in Fig. S4(c), which also shows that  $S_N \sim \ln(L)$ .

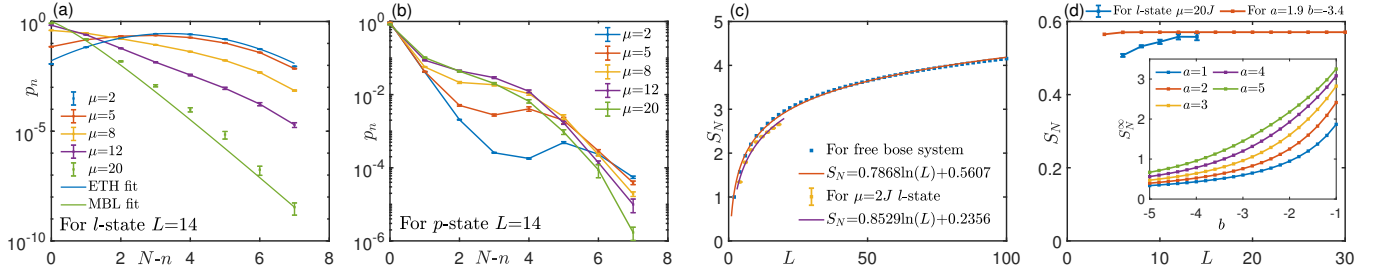


FIG. S4. The  $p_n$  distribution of the stationary state for a  $L = 14$  dBH chain with different disorder strengths. (a) is for the initial  $l$ -state, under the case of  $\mu = 2$ , fitted by a Gaussian distribution; for  $\mu = 20$ , the distribution is fitted by  $p_{n_r} = (n_r + 1)^a e^{bn_r+f}$  with  $a = 1.9$  and  $b = -3.4$ , where  $n_r = N - n$  denotes the number of particles in the right half-chain. (b) is for the initial  $p$ -state. (c) The logarithmic fit of the particle number entropy  $S_N$  with chain length for the stationary state with the initial  $l$ -state and the small disorder. A comparison of the logarithmic fit to the ideal case of the free Bose system is also given. (d) Area law of the particle number entropy  $S_N$  for the stationary state when the initial state is  $l$ -state and large disorder, and the inset gives the results of  $S_N$  with parameters from the phenomenological analysis of an infinitely long chain. All calculations related to entropy in the figure have taken 2 as the logarithmic base.

For the case of large disorder, the system is in MBL, as shown in Fig. S4(a). In this case,  $p_{n_r}$  can be fitted with an exponential decay-like function with  $p_{n_r} = (n_r + 1)^a e^{bn_r+f}$ , where  $b$  is always less than 0 and the larger the disorder, the smaller  $b$  will be. Using the normalization condition of  $p_{n_r}$ , we can obtain  $p_{n_r} = \frac{(n_r+1)^a e^{b(n_r+1)}}{\left[ Li_{-a}(e^b) - (e^b)^{2+N} L(e^b, -a, 2+N) \right]}$ , where  $Li_{-a}(e^b)$  is Lerch zeta function, and  $L(e^b, -a, 2+N)$  is polylogarithm function. In Fig. S4(d), the calculation of  $S_N$  using the normalized  $p_{n_r}$  values is given, which can be seen to behave as an area law. When the chain length is infinite, we can get  $p_{n_r} = (n_r + 1)^a e^{bn_r} \frac{e^b}{Li_{-a}(e^b)}$ . Taking this  $p_{n_r}$  to compute  $S_N^\infty$ , turning the summation of which into an integral, a complex analytic expression can be obtained. In the inset of Fig. S4(d),  $S_N^\infty$  is calculated using numerical integration, and it can be seen that as the disorder increases (i.e.,  $b$  decreases),  $S_N^\infty$  becomes smaller, and the tendency of  $S_N^\infty$  to become smaller slows down when the disorder is large, which indicates that the eventual entropy does not decrease continuously to zero as the disorder increases.

## Supplemental Note 7. Miscellaneous others

Figure S5 below provides additional evidence to support the single-logarithmic temporal growth for the total configuration entropy  $S_C(t)$  inside the scatter MBL regime. Similar single-log  $S_C$  growth has also been given by Fig. 4(d) in the main text. Here, we choose the disorder strength to be slightly smaller, i.e.,  $\mu = 12J$ , and the initial state to be the  $l$ -state. Via a systematic finite-size scaling analysis which covers the length range from  $L = 6$  to  $L = 14$ , it has been clearly demonstrated that the saturated values of  $S_C(t = \infty)$  satisfy the expected volume scaling law.

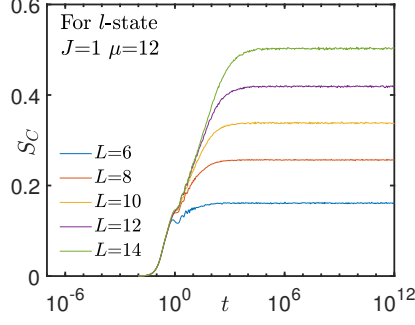


FIG. S5. The single-log temporal growth of the total configuration entropy  $S_C$  in the scatter MBL phase realized upon a significant disorder strength  $\mu = 12J$  and by initializing the chain in the  $l$ -state. The finite-size analysis based on a series of  $L$  shows that the saturation values of  $S_C$  at infinite time fulfil a volume scaling law.

To supply further insights for the energy-resolved dynamical phase diagram of the dBH chain model from the perspective of Hilbert-space (de)localization, in Fig. S6 we study the preliminary time evolutions of the inverse participation ratios (IPRs) for the three types of MBL regimes in the phase diagram that are realizable by starting from the initial  $p$ - and  $l$ -states respectively under different values of the disorder strength  $\mu$ . MBL is typically signalled by the vanishing of IPR, and we find this is indeed the case for both scatter and cluster MBLs, where the absolute values of IPRs have already been smaller than  $10^{-3}$  for a finite, periodic dBH chain with length  $L = 12$ .

The two insets in Fig. S6 plot the corresponding saturated values of IPRs at the infinite-time limit for the respective initial  $l$ - and  $p$ -states as a function of the disorder strength  $\mu$ . Interestingly, for the lower inset which describes the results for the initial  $p$ -state, we notice that the profile of the infinite-time IPR shows an emerging peak at about  $\mu = 10J$ , signalling that there might exist a transition between the hard cluster MBL at small  $\mu < 10J$  and the soft cluster MBL at large  $\mu > 10J$ . While, for the initial  $l$ -state, the upper inset demonstrates that the scatter thermal and the scatter MBL phases form two independent plateaus. The thermal one is centering around a finite value for the infinite-time IPR. By contrast, the infinite-time IPR approaches zero when getting deep inside the scatter MBL regime. In between, there exists a sharply decreasing line connecting these two plateaus, which roughly indicates the transition zone in the infinite-time IPR diagram.

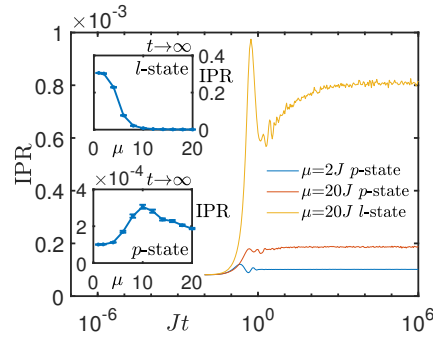


FIG. S6. Temporal evolutions of IPRs for the three types of MBL regimes in the dBH chain. The length of the periodic chain is  $L = 12$ . The two insets give the corresponding saturation values of IPRs at infinite time for the initial  $l$ - and  $p$ -states as a function of the disorder strength  $\mu$ . Particularly, a peak is observed in the lower inset for the initial  $p$ -state, which might serve as a transition signature between the hard and the soft cluster MBL phases. Notice, however, once the system is fully localized, the absolute values of IPRs are normally small.